Theses, Dissertations and Culminating Projects

8-2021

Computational Analysis to Study the Efficiency of Shear Activated Nano-Therapeutics in the Treatment of Atherosclerosis

Nicholas Jefopoulos
Montclair State University

Abstract

Strokes are the fifth leading cause of death in the United States and can cause long-term disabilities in patients who survive a stroke. The vast majority of these strokes are ischemic, primarily caused by intracranial atherosclerosis. Most therapies to combat intracranial atherosclerosis simply manage it and do not remove the buildup of plaque. Targeted shear-activated nanotherapeutics are currently being developed to remove these plaques. We discuss the roles that aggregate particle density, aggregate particle diameter, vessel geometry, stenosis shape and breakup threshold play in the efficiency of this new technology. Computational studies were performed to test these parameters in three idealized vessels with varying curvatures (straight, quarter-circle, semi-circle) and two different stenosis shapes (concentric, eccentric). We find that curvature plays a large role in the breakup threshold. The optimal breakup threshold for a semi-circular shaped vessel is 4.5 times that of a straight vessel, yet the less curved quarter-circle shaped vessel has an optimal breakup threshold that is 6.3 times that of the straight vessel. Therefore, no quantifiable pattern was discovered between geometry curvature and optimal threshold value. Curvature also plays a large role in how particle diameter affects the efficiency of these nanotherapeutics. Although the effects of particle size between 1 and 5 μm is minimal, the optimal particle diameter for a straight vessel was located at the smallest end of the tested range while the optimal diameter for the curved case was located at the largest end of the tested range. Particle specific density was explored and found to have a negligible effect. Finally, curvature and stenosis location (superior, inferior, and ventral/dorsal) play a large role in optimizing breakup position. It is optimal for the stenosis to be in the path of the aggregate particle.

MONTCLAIR STATE UNIVERSITY

Computational Analysis To Study The Efficiency of Shear Activated
Nano-Therapeutics in The Treatment of Atherosclerosis

by

Nicholas Jefopoulos

A Master's Thesis Submitted to the Faculty of

Montclair State University

In Partial Fulfillment of the Requirements

For the Degree of
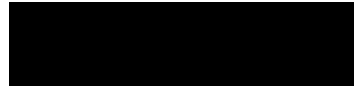
Master of Science

August 2021

College of Science and Mathematics

Department of Applied
Mathematics and Statistics

Thesis Committee:

Dr. Bong Jae Chung
Thesis Sponsor

Dr. Eric Forgoston
Committee Member

Dr. Ashuwin Vaidya
Committee Member

COMPUTATIONAL ANALYSIS TO STUDY THE EFFICIENCY OF SHEAR ACTIVATED NANO-THERAPEUTICS IN THE TREATMENT OF ATHEROSCLEROSIS

A THESIS

Submitted in partial fulfillment of the requirements

For the degree of Master of Science

by

NICHOLAS JEFOPOULOS

Montclair State University

Montclair, NJ

2021

Acknowledgements

Contents

List of Figures

List of Tables

1 Introduction

Every year in the United States 795,000 people suffer from a stroke, which is a governing cause of long-term disability and the fifth leading cause of death in the country [1,2]. Approximately 85% of all strokes are ischemic (blockage in blood flow), and intracranial atherosclerosis is a leading cause of ischemic stroke [1,3]. Approximately 50% of ischemic strokes occur within the middle cerebral artery (MCA) region [1]. The MCA is positioned within a connection of several arteries located in the brain's inferior region known as the Circle of Willis (CoW) [4]. Plaque formation within the CoW is primarily consigned to its large arteries which includes the MCA [3].

In addition to the prevalence of strokes, a connection between strokes and other disease necessitates research into medical prevention measures. Intracranial atherosclerosis and ischemic stroke are also risk factors to the development of dementia [3]. A link has been established between atherosclerosis within the CoW and Alzheimer's Disease [5]. Hypoperfusion due to CoW plaques could be the contributing factor, as considerable widespread pathologic hemodynamic changes in the brain have been observed in Alzheimer's Disease patients [5]. This seems reasonable considering the CoW supplies 80% of the oxygenated blood to the cerebrum, whose functions include reasoning and problem solving [1].

Antithrombotic therapy, risk factor modification, and lipid-lowering treatments, along with more invasive stenting and bypass surgeries, are all currently being used to treat intracranial atherosclerosis [6]. Apart from healthy lifestyle changes, all of these treatments are not without their risks and most do not attempt to remove plaque from arteries. Among the noninvasive treatments, antithrombotic therapy, the use of an antiplatelet or anticoagulant to reduce clotting, comes at the risk of increased bleeding [7]. Lipid-lowering treatments use statins to lower overall cholesterol to slow down the buildup of plaques with possible risk of liver damage and development of type II diabetes [8].

A therapy that is effective in dissolving plaque from arteries is necessary for treating patients at risk of experiencing a stroke. Targeted nanotherapeutics have increasingly been developed and used to dissolve malignant tumors [9]. Specifically targeted nanotherapeutics that take advantage of mechanical forces may be a novel method to attack atherosclerosis in the future. Thrombosed vasculature displays mechanical characteristics which differ from normal blood vessels. In a thrombosed vasculature, the local fluid shear stress (caused mainly by friction) may increase greatly, from under 70 $dyne/cm^2$ to greater than 1,000 $dyne/cm^2$ ($1\ dyne = 1 \times 10^{-5}\ N$) [10].

The high fluid shear stress in these locally stenosed regions activates platelets which quickly adhere to the vessel, causing narrowing. Activation of platelets through high fluid shear stress is a major contributing factor to the development of atherosclerotic plaques. Korin et al., as described in their 2012 paper, developed a shear stress activated nano-therapeutic (SA-NT) inspired by platelet shear stress activation to target atherosclerotic plaques [10]. The therapeutic consists of particles that are approximately the size of platelets, between one and five micrometers in diameter. Each particle is an aggregate consisting of smaller nanoparticles. The therapeutic remains intact during normal flow conditions but breaks up into their smaller components

when exposed to higher levels of fluid shear stress. These smaller nanoparticles will experience lower drag forces and consequently have greater adherence to the stenosis allowing the therapeutic to be locally targeted and dissolve the atherosclerosis.

These SA-NTs are constructed by spray-drying solutions of poly-lactic-co-glycolic acid (PLGA) to form a micrometer sized aggregate composed of smaller nanoparticles. Most other current therapeutics work to stop plaque growth instead of dissolving it, as the SA-NT is designed to do . The great benefit of using targeted SA-NTs is the ability to use a much smaller dosage without compromising effectiveness. It was shown that to clear a pulmonary embolism within mice, this method used 1/100 the normal dose [10]. SA-NTs, in conjunction with temporary endovascular bypass, have been shown to achieve high rates of recanalization without the dangers of vascular trauma seen in stent-retriever thrombectomies [11].

While targeting atherosclerosis with high dosage therapeutics is desirable, studies must be conducted to ensure that unwanted side effects are minimized through effective aggregate breakup. Korin et al. determined a shear stress threshold of $100\ dyne/cm^2$ [10]. Nanoparticles breaking off from the aggregate at this, or higher, shear stress intensity or higher were detected at levels that are an 8-12 fold increase as compared to the levels detected under normal shear stress conditions. Using computational fluid dynamics (CFD), they equated this shear stress level to a 60% obstructed vessel. Normal vessels experience a typical level of shear stress of approximately $10-30\ dyne/cm^2$ [10]. Aggregate particle parameters that will allow targeting of vessels less than 60% obstructed is a practical pursuit, as narrowing of 50% to 69% is considered moderate and may require aggressive treatment, especially if the patient is showing symptoms of the disease [12, 13].

Numerical studies have been conducted to determine the effect of certain parameters of particles in the bloodstream, which aid in drug development. These parameters were primarily studied to give insight to particle binding which may contribute to the retention of large amounts of toxic particles. Doig et al. studied the influence of particle size compared to average particle residence time in a bifurcated carotid artery using numerical methods [9]. Using an arterial geometry with a diameter of approximately $0.34\ cm$, the conclusion was that particle size and mean residence time are positively correlated, with the maximum residence time dropping sharply with a reduction in particle size. However, as the particle diameter decreased, the number of particles experiencing wall interactions increased. The test was also run for an arteriole geometry with a diameter of approximately $0.0034\ cm$. The smaller size allowed Brownian motion to be a larger factor, and the residence time increased by 3% when reducing the particle size from $500\ nm$ to $50\ nm$ [9].

Studies concentrating on SA-NTs and how different parameters influence their breakup have not yet been fully conducted. Additionally the applicability of SA-NTs in the treatment of atherosclerosis in the CoW is not fully understood [10]. The roles that particle density, particle diameter, vessel geometry, stenosis shape, and breakup threshold (shear rate) play in the effectiveness of SA-NTs have not been studied extensively. This study seeks to investigate these parameters and their influence on aggregate breakup position and rate using numerical modeling techniques. For SA-NTs to work as intended, enough of the aggregate must break up at the stenosis.

Breakup before or after will not be effective in treating atherosclerosis and could have potentially harmful effects. We will explore the effect of the parameters on breakup position and rate using several idealized arterial geometries. Each geometry will have one of three curvatures and either a concentric or eccentric stenosis.

2   Methods

The computational method involves a number of steps, which we now broadly describe. Details of each step are described in the subsections which follow. The numerical simulations begin by creating idealized arterial geometries. Flow data, in the form of a velocity field, is then calculated using the Navier-Stokes equation for each geometry. A force balance equation is solved using a combination of investigated parameters to determine particle trajectories. The aggregate particle model consists of twenty-five nanoparticles attached to the surface of each aggregate particle. Each nanoparticle has an 1.8×10^{-5} cm diameter which matches the diameter of the nanoparticles in Korin, et al.'s 2012 paper [10]. Once a breakup threshold has been met, in this case once the particle reaches a certain angular velocity, the aggregate particle will break up and its components are tracked as they disperse through the flow. Figure 1 outlines the computation method.

A total of seven arterial geometries were evaluated. These seven are idealized geometries, with each possessing one of three curvatures. All of the idealized geometries represent a vessel with a diameter of 0.5 cm and a length of 7.0 cm. The flow enters each geometry in a single inlet and exits using a single outlet. Geometry curvatures are either a straight pipe (R_1), a 7.0 cm segment of a 44.56 mm radius torus, i.e., a quarter of a torus (R_2), or a 7.0 cm segment of a 22.28 mm radius torus, i.e., a half of a torus (R_3). Concentric or eccentric (off-center with respect to width) stenoses were created within the center (with respect to length) of each geometry. For the R_1 and R_3 vessels, a unique geometry with 50% occlusion (0.25 cm opening) was created for each combination of stenosis characteristics (concentric or eccentric; and occlusion). In the eccentric R_3 case, superior, inferior, and ventral/dorsal locations also are studied. Figure 2 shows a selection of the arterial geometries and Table 1 gives a listing of all idealized geometries tested. The inclusion of concentric and eccentric stenoses is due to their dual prevalence in the CoW. One study of 1,220 CoW segments found
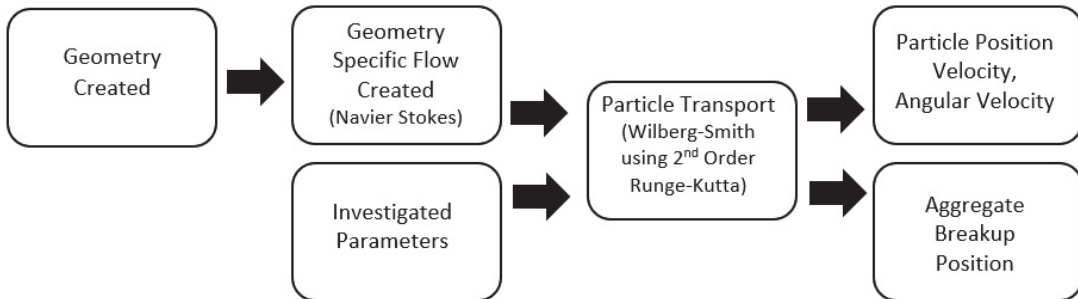
Figure 1: Overview of the computational method.
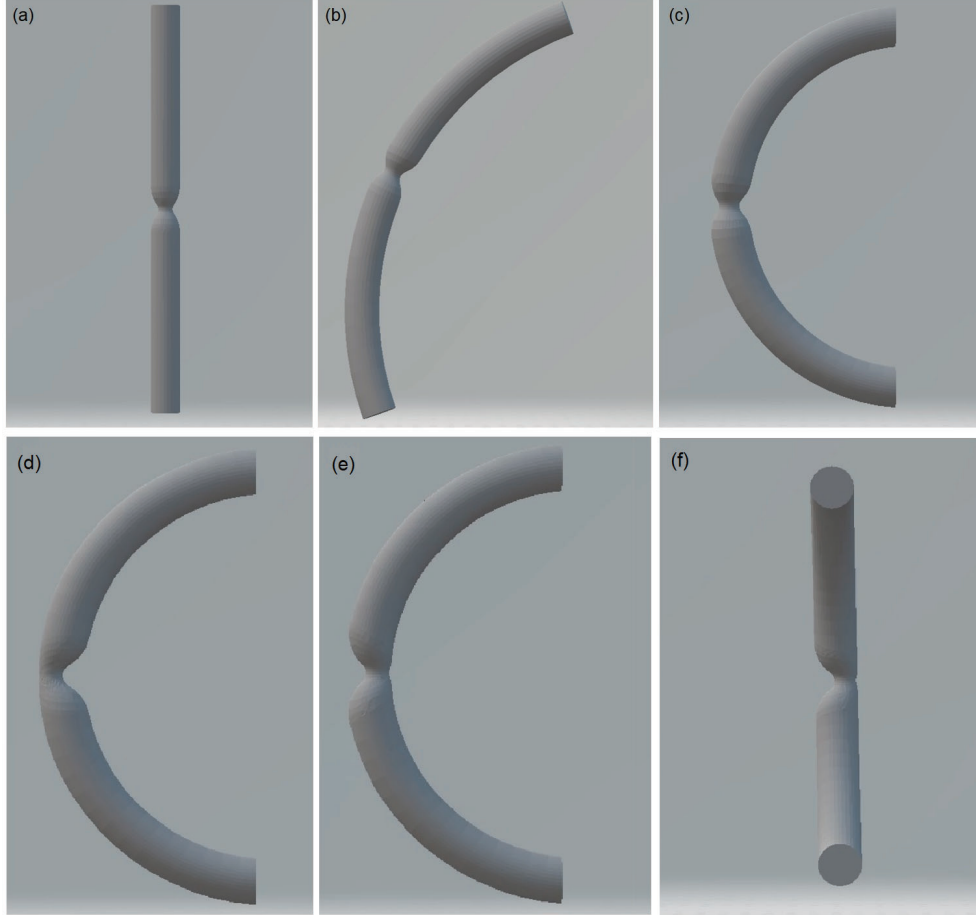
Figure 2: Idealized Geometries. (a) R_1 geometry with concentric 50% occlusion. (b) R_2 geometry with concentric 50% occlusion. (c) R_3 geometry with concentric 50% occlusion. The remaining (d,e, and f) images show the R_3 geometry with eccentric stenosis in the (d) superior, (e) inferior, and (f) ventral/dorsal locations.

that 79% of advanced plaques were eccentric and 19% were concentric. The other 2% were completely occluded plaques [3]. All seven idealized geometries were created using FreeCAD software version 0.18 and used a .stl file for CFD analysis to assess blood flow data [14].

2.1   Computational Fluid Dynamics (CFD) Analysis

We triangulate the idealized geometries using in-house software for segmentation/model construction (ZMD). Each model is then used as a surface to generate a finite element grid based on an advancing front method. The method uses in-house software (GEN3D) to re-triangulate the surface and generate tetrahedral elements [15, 16].

Number	Vessel Geometry	Stenosis Shape	Stenosis Location
1	R_1	Concentric	NA
2	R_1	Eccentric	NA
3	R_2	Concentric	NA
4	R_3	Concentric	NA
5	R_3	Eccentric	Inferior
6	R_3	Eccentric	Superior
7	R_3	Eccentric	Ventral / Dorsal

Table 1: Overview of the vessel geometries, stenosis shapes, and stenosis locations that were tested.

Unsteady Navier-Stokes equations are used to model blood flow with Newtonian fluid properties (density, $\rho = 1.105 \ g/cm^3$ and viscosity, $\mu = 0.04 \ Poise$). The equations are as follows:

$$\nabla \cdot \vec{v} = 0, \tag{1}$$

$$\rho(\frac{\partial \vec{v}}{\partial t} + \vec{v} \cdot \nabla \vec{v}) = -\nabla P + \mu \nabla^2 \vec{v}, \tag{2}$$

where v is the flow velocity. The unsteady flow equations are solved with in-house software that utilizes a fully implicit scheme and efficient solution algorithms (FE-FLO) [17, 18]. A traction-free boundary condition at the outlet is implemented. Vessel wall compliance (ability to distend) is neglected for this study and thus, no-slip boundary conditions are imposed at the walls.

2.2 Particle Trajectories

To attain aggregate and nanoparticle position as well as translational and rotational (angular) velocities, a force balance equation was used. Using Newton's 2nd law $ma = F$, one has

$$S\frac{d\vec{v}_p}{dt} = \vec{F}_{AM} + \vec{F}_B + \vec{F}_D + \vec{F}_L, \tag{3}$$

where S is the specific density of the particle (ratio of particle density and fluid density) , $\frac{d\vec{v}_p}{dt}$ is the acceleration of the particle, $\vec{F}_{AM}$ is the force of added mass, $\vec{F}_B$ is the Bassett force, $\vec{F}_D$ is the drag force and $\vec{F}_L$ is the lift force [19]. Substitution of the specific forms of these forces leads to the following force balance equation:

$$S\frac{d\vec{v}_p}{dt} = \frac{D\vec{u}}{Dt} + \frac{1}{2}\left(\frac{D\vec{u}}{Dt} - \frac{d\vec{v}_p}{dt}\right) + \frac{3}{4}\frac{C_D}{D}|\vec{u} - \vec{v}_p|(\vec{u} - \vec{v}_p) + \vec{f}_{\text{lift}}, \tag{4}$$

$$\vec{f}_{\text{lift}} = \vec{f}_{\text{lift:shear}} + \vec{f}_{\text{lift:rotational}}, \tag{5}$$

9

where $\frac{D}{Dt}$ is the material derivative, $\vec{u}$ is the velocity field, C_D is the coefficient of drag, D is the diameter of the particle, $|\cdot|$ denotes the magnitude of the vector, $\vec{f}_{\text{lift:shear}}$ is the shear-induced lift force and $\vec{f}_{\text{lift:rotational}}$ is the rotation-induced lift or "Magnus force".

This force balance equation is solved using the second-order Runge-Kutta method (midpoint method). This technique approximates the solution of the second-order Taylor expansion without needing to compute derivatives of $f(t, y)$. After aggregate breakup, each nanoparticle is also governed by Brownian motion due to its small size and thus, we add motion in the form of a scaled pseudo-random vector to the position of each nanoparticle.

2.3   Interpolation of Flow Data

The CFD analysis produces flow data at every 0.01 seconds. It generates 100 snapshots of flow data including flow velocities and pressures for each cardiac cycle of 1 second. In order to reduce our computational costs for the CFD analysis, the flow data is interpolated into smaller time step sizes.

The binary output files are quite large, ranging from approximately 10 MB to 40 MB. This file size made it prudent to develop code to interpolate the flow data within the model rather than creating larger output files. The time step size for the simulation of particle trajectories is determined by a convergence test, which will be discussed in the results section.

The subroutine interpolates the data linearly using

$$t = t_0 + i\frac{t_1 - t_0}{s}, \tag{6}$$

$$\vec{u} = \vec{u}_0 + (t - t_0)\frac{\vec{u}_1 - \vec{u}_0}{t_1 - t_0}, \tag{7}$$

where $\vec{u} = (u, v, w)$ and t are the interpolated velocity and time respectively, $\vec{u}_0 = (u_0, v_0, w_0)$, and t_0 are the velocities and time from an output file, and $\vec{u}_1 = (u_1, v_1, w_1)$, and t_1 are the velocities and time from the preceding output file, s is the number of interpolated data points between two original data points, and $\{i \in \mathbb{Z} | 1 \le i \le s\}$. The appropriate time step was computed from the convergence test to be 0.002 of the original 0.01 seconds. This algorithm does not store any of the interpolated data after each iteration in order to minimize computer memory usage.

2.4   Initial Conditions

Aggregate particles are allocated every 50 elements on a plane 0.05 cm from the geometry inlet. The number of elements between aggregate particles was chosen arbitrarily. The number of aggregate particles in the test and their position is dependent on the number of triangular elements that make up the inlet. This method produces between 10 and 20 particles for each geometry. After aggregate particles break up into their nanoparticle components the aggregate particle is still tracked in the flow as if it had not broken up for the possibility of gaining further insight.

10

2.5 Particle Ricochet Assumption

The computational method allows particles to exit the geometry at any point in a cycle. Therefore, a method had to be devised to prevent a particle, aggregate or nano-, from leaving the domain through the arterial vessel wall. We assume that a particle hitting the vessel walls is bounced back to the luminal region so that: 1) the particle motion obeys the linear momentum conservation law by considering the walls are rigid and 2) there are no biochemical reactions between the walls and particle. To ensure that particles do not leave the geometric domain prematurely, we have developed a ricochet method that enables particles to exit the outlet.

If $\vec{v}$ is the incident vector, $\hat{n}$ is the normal vector to the surface at the point at which $\vec{v}$ hits, then the reflected vector $\vec{w}$ is described by

$$\vec{w} = 2\hat{n}(\vec{v} \cdot \hat{n}) - \vec{v}. \tag{8}$$

The reflected vector has an angle of reflection that is the same as the angle of incidence.

If a particle leaves the geometry domain but did not exit through the geometry outlet during a time step iteration, the algorithm creates a line between the particle's position at the previous time step and the particle's current position outside the domain. This line consists of 100,000 equally spaced points. The geometric boundaries used in our study are comprised of triangular elements. The centroid (geometric center) of each triangular element and the distance between every point on the created line and every element's centroid is calculated, and the minimum distance is determined. The centroid with the minimum distance from the line is then used to create a unit normal from the surface. Vector $\vec{v}$ is then calculated by finding the component wise distance from the original position (x_1, y_1, z_1) to the centroid and normalized
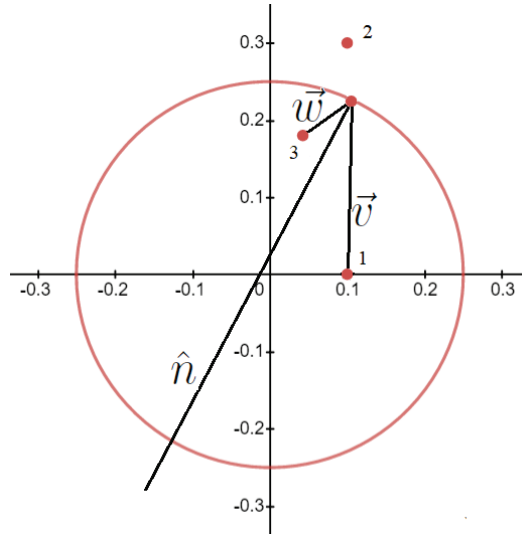
Figure 3: Geometry of the particle ricochet subroutine. The particle (position 1) has moved outside the domain to position 2. This routine moves the particle back into the domain to a point (position 3) of reflection off the boundary.

by its magnitude. The reflection vector is scaled by the distance from the geometry surface to the particle's current position outside the domain (x_2, y_2, z_2). Vector $\vec{w}$ is calculated using Eq. 8, scaled, and added to the centroid vector to determine the new position of the particle.

2.6   Convergence Test

A convergence test was performed to determine a time step at which the discretization error is minimal. A straight arterial vessel with diameter of 0.5 cm and length of 7.0 cm was used as the geometry for this test. It contained a concentric stenosis at its center with a maximum narrowing of 0.25 cm. Eighteen particles were simultaneously tracked, each having a different arbitrary starting position. This test was performed eleven times, starting with the original time step from the binary flow data of 0.01 seconds and dividing that time step in half for each study thereafter. For each particle, the radial position data was collected from each study. Figure 4 shows the convergence test of a single aggregate particle moving through the R_1 geometry with 50% occlusion.

A comparison of particle position for each particle every 0.01 seconds was made between each consecutive study. The maximum difference between position data was calculated and normalized using the geometry's radius of 0.5 cm. Using an error threshold of 0.001, it was determined that the difference between study 10 (0.01 $s/512$) and study 11 (0.01 $s/1024$) met the convergence threshold requirements for all particles except one (MP$_8$). It was observed that the majority of maximum position differences were located near the outlet of the geometry. Since this study
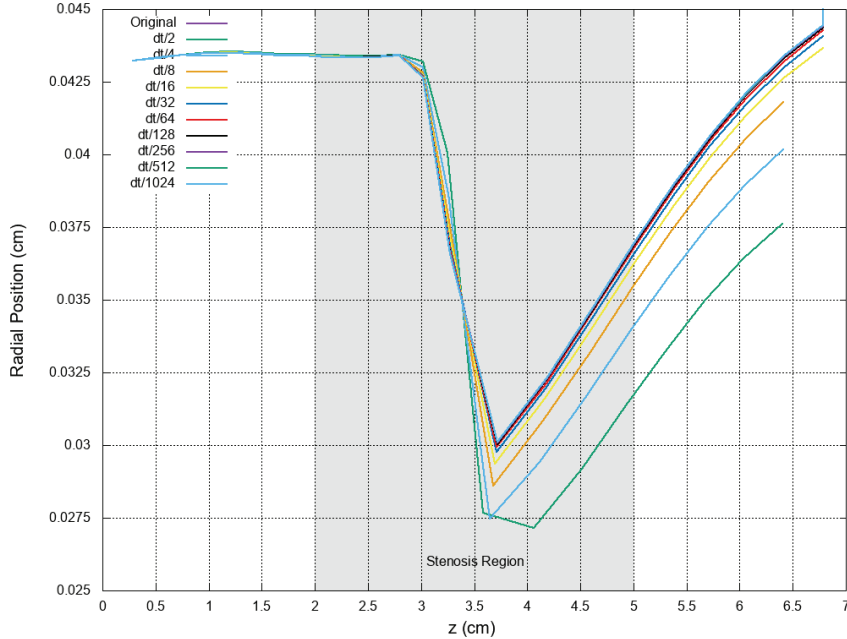
Figure 4: Convergence test of a single aggregate particle moving through R_1 geometry with concentric 50% occlusion.

is concerned with the region around the stenosis it was sensible to define a stenosis region and restrict the data analysis to it. The stenosis region is defined as being 1.5 cm before and after the center of the stenosis at 3.5 *cm* from the inlet. Tables 2 and 3 compare the maximum position with all data and the maximum position contained around the stenosis.

From 2.0 *cm* to 5.0 *cm* from the inlet, all particles met the threshold requirement between study 10 and 11. Therefore 0.01/512 was determined to be the time step for this model. We use the time step for the rest of our simulations. In conducting the convergence study an interesting correlation was found between initial radial position of the aggregate particle and the normalized maximum difference between position data of the dt/512 versus dt/1024 case. It appears that particles positioned farther away from the stenosis center had a greater gap between the dt/512 and dt/1024 cases, as seen in Figure 5.

| Study	1	2	3	4	5	6	7	8	9	10
Data Set 1	Original	DT/2	DT/4	DT/8	DT/16	DT/32	DT/64	DT/128	DT/256	DT/512
Data Set 2	DT/2	DT/4	DT/8	DT/16	DT/32	DT/64	DT/128	DT/256	DT/512	DT/1024
Particle					Normalized Δr					
1	9.03E-02	2.71E-02	2.24E-02	1.29E-02	1.00E-02	4.90E-03	2.39E-03	1.29E-03	6.07E-04	9.83E-04
2	6.85E-02	3.05E-02	2.49E-02	1.48E-02	7.73E-03	4.90E-03	2.72E-03	1.90E-03	9.65E-04	4.91E-04
3	1.81E-01	4.36E-02	3.05E-02	1.70E-02	9.13E-03	6.19E-03	3.32E-03	2.56E-03	1.61E-03	8.13E-04
4	5.33E-02	5.68E-02	3.19E-02	1.79E-02	8.26E-03	3.80E-03	1.83E-03	8.99E-04	6.46E-04	3.65E-04
5	2.05E-02	1.12E-02	6.62E-03	3.42E-03	1.79E-03	9.27E-04	4.68E-04	2.37E-04	1.21E-04	5.99E-05
6	1.39E-02	1.03E-02	5.78E-03	2.95E-03	1.47E-03	7.34E-04	3.77E-04	1.90E-04	9.48E-05	4.59E-05
7	5.15E-02	6.04E-02	3.37E-02	1.68E-02	7.86E-03	3.87E-03	1.88E-03	9.16E-04	4.62E-04	2.34E-04
8	1.58E-01	3.13E-02	4.02E-02	2.12E-02	4.42E-02	3.56E-02	1.33E-02	5.65E-03	3.83E-03	1.54E-03
9	6.12E-02	5.74E-02	3.68E-02	1.88E-02	9.39E-03	4.60E-03	2.31E-03	1.19E-03	6.52E-04	2.98E-04
10	2.40E-02	1.38E-02	7.30E-03	4.10E-03	2.17E-03	1.06E-03	5.26E-04	2.67E-04	1.36E-04	7.45E-05
11	1.03E-02	5.12E-03	3.22E-03	1.63E-03	8.10E-04	4.15E-04	2.08E-04	1.05E-04	5.16E-05	2.64E-05
12	2.24E-02	1.14E-02	6.30E-03	3.41E-03	1.73E-03	8.89E-04	4.46E-04	2.24E-04	1.12E-04	5.73E-05
13	7.69E-02	7.06E-02	3.51E-02	2.05E-02	9.92E-03	5.15E-03	2.46E-03	1.24E-03	6.08E-04	3.08E-04
14	1.07E-01	6.20E-02	3.07E-02	3.52E-02	1.87E-02	8.85E-03	3.87E-03	1.88E-03	8.86E-04	4.34E-04
15	8.02E-02	2.71E-02	3.72E-02	2.42E-02	1.55E-02	9.58E-03	4.74E-03	2.90E-03	1.43E-03	7.35E-04
16	5.71E-02	3.49E-02	1.98E-02	1.26E-02	5.73E-03	3.02E-03	1.49E-03	7.51E-04	3.77E-04	1.86E-04
17	9.08E-02	5.80E-02	2.98E-02	1.57E-02	7.56E-03	3.66E-03	1.82E-03	8.96E-04	4.48E-04	2.32E-04
18	1.50E-01	2.46E-02	2.81E-02	2.54E-02	1.17E-02	7.01E-03	3.50E-03	1.72E-03	8.56E-04	4.25E-04

Table 2: Convergence Test: Normalized Δr by study (all data). Cells highlighted in blue meet the threshold requirement.

Study	1	2	3	4	5	6	7	8	9	10
Data Set 1	Original	DT/2	DT/4	DT/8	DT/16	DT/32	DT/64	DT/128	DT/256	DT/512
Data Set 2	DT/2	DT/4	DT/8	DT/16	DT/32	DT/64	DT/128	DT/256	DT/512	DT/1024
Particle					Normalized Δr					
1	9.03E-02	2.71E-02	2.20E-02	9.04E-03	4.79E-03	2.25E-03	1.01E-03	5.06E-04	5.88E-04	9.83E-04
2	6.85E-02	2.08E-02	2.48E-02	1.48E-02	7.73E-03	4.23E-03	2.07E-03	1.06E-03	5.26E-04	2.64E-04
3	1.81E-01	4.29E-02	3.05E-02	1.70E-02	9.13E-03	4.73E-03	2.52E-03	1.28E-03	6.45E-04	3.17E-04
4	5.33E-02	4.23E-02	2.32E-02	1.37E-02	6.57E-03	3.17E-03	1.55E-03	7.75E-04	3.86E-04	1.90E-04
5	2.05E-02	1.05E-02	6.16E-03	3.38E-03	1.79E-03	9.27E-04	4.68E-04	2.37E-04	1.21E-04	5.35E-05
6	1.39E-02	1.03E-02	5.78E-03	2.95E-03	1.30E-03	6.38E-04	3.28E-04	1.63E-04	8.14E-05	3.96E-05
7	5.15E-02	4.66E-02	2.56E-02	1.38E-02	6.70E-03	3.34E-03	1.65E-03	8.13E-04	4.09E-04	2.10E-04
8	1.58E-01	3.13E-02	4.02E-02	2.12E-02	1.16E-02	5.63E-03	2.82E-03	1.40E-03	7.04E-04	3.71E-04
9	6.12E-02	4.88E-02	3.24E-02	1.79E-02	9.12E-03	4.60E-03	2.31E-03	1.14E-03	5.73E-04	2.92E-04
10	2.40E-02	1.35E-02	7.03E-03	3.91E-03	2.02E-03	9.88E-04	4.92E-04	2.49E-04	1.27E-04	7.45E-05
11	1.03E-02	5.12E-03	3.00E-03	1.57E-03	7.61E-04	3.90E-04	1.96E-04	9.88E-05	4.86E-05	2.46E-05
12	2.24E-02	1.14E-02	6.30E-03	3.34E-03	1.69E-03	8.64E-04	4.34E-04	2.18E-04	1.09E-04	5.43E-05
13	7.69E-02	6.59E-02	3.31E-02	1.99E-02	9.79E-03	5.15E-03	2.46E-03	1.24E-03	6.08E-04	3.08E-04
14	9.47E-02	6.20E-02	3.07E-02	2.06E-02	1.35E-02	6.28E-03	2.98E-03	1.43E-03	7.33E-04	3.33E-04
15	8.02E-02	2.71E-02	3.72E-02	2.11E-02	1.17E-02	5.71E-03	2.79E-03	1.39E-03	7.37E-04	3.67E-04
16	5.30E-02	2.95E-02	1.59E-02	9.21E-03	4.24E-03	2.31E-03	1.15E-03	5.79E-04	2.89E-04	1.42E-04
17	8.21E-02	4.88E-02	2.51E-02	1.38E-02	6.83E-03	3.39E-03	1.70E-03	8.36E-04	4.19E-04	2.20E-04
18	1.45E-01	2.46E-02	2.81E-02	2.02E-02	1.08E-02	5.43E-03	2.68E-03	1.30E-03	5.65E-04	2.83E-04

Table 3: Convergence Test: Normalized Δr by study (stenosis region). Cells highlighted in blue meet the threshold requirement.
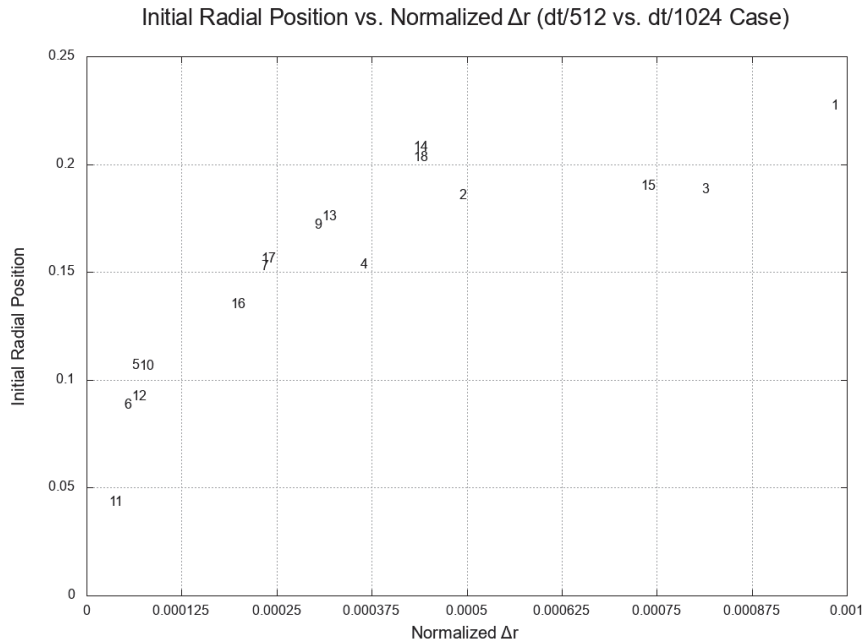

Figure 5: Convergence test showing the positive correlation between initial radial particle position and normalized maximum difference between position data of dt/512 vs dt/1025 cases.

3   Results

3.1   Optimal Breakup Threshold

Angular velocity, ω, was used as a breakup threshold for aggregate particles. When the aggregate particles reach an angular velocity threshold, they break up into their nanoparticle components. Once an aggregate particle is broken, the twenty five nanoparticles will break off with the same velocity and angular velocity as the aggregate particle had just prior to breakup as shown in Figure 6. To determine a breakup threshold, the angular velocity at time step, $t = 1$, was calculated for each aggregate particle. The minimum angular velocity, ω_{min}, was determined, and different breakup thresholds were generated by scaling ω_{min} to a variety of magnitudes. To determine the optimal breakup threshold for each study, two criteria were measured: the percentage of particles that broke up within the stenosis region and the average distance the aggregate particle broke up from the center of the stenosis. This average includes all aggregate particles, including those that did not break up within the stenosis region as well as those that broke up before and after the stenosis.

For the R_1 and R_3 geometries, we chose the stenosis region to be 1 cm before and 1 cm after the center of the stenosis along the z-axis. This a slightly smaller region than the region used in our original convergence test. The stenosis region on the R_2 geometry consisted of the area spanning 0.5 cm before and 0.5 cm after the center of the stenosis. The shorter region is due to the stenosis lying on a slant relative to the z-axis. The average breakup distance from the center of the stenosis was ascertained by capturing the position of the first appearance of a nanoparticle from each aggregate particle. Due to time and post processing limitations, data from
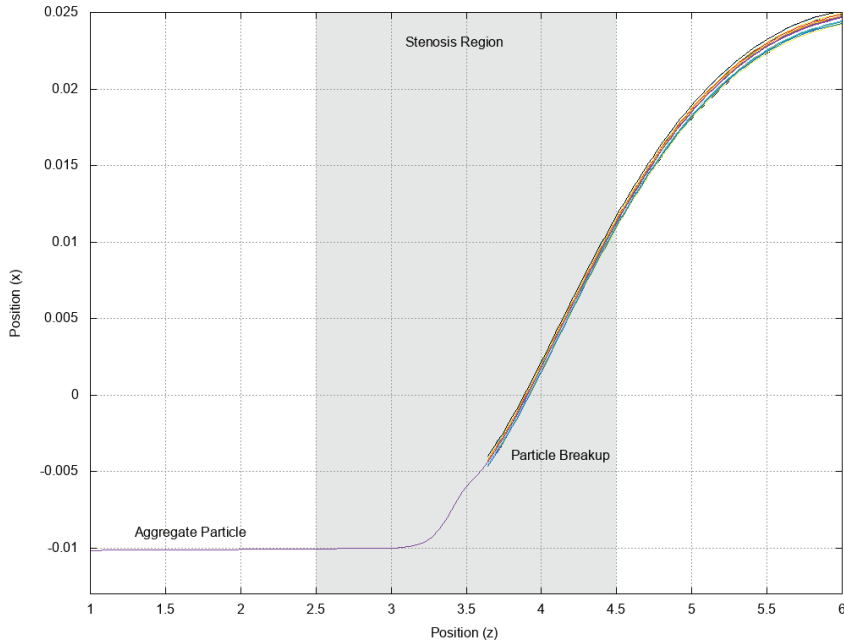

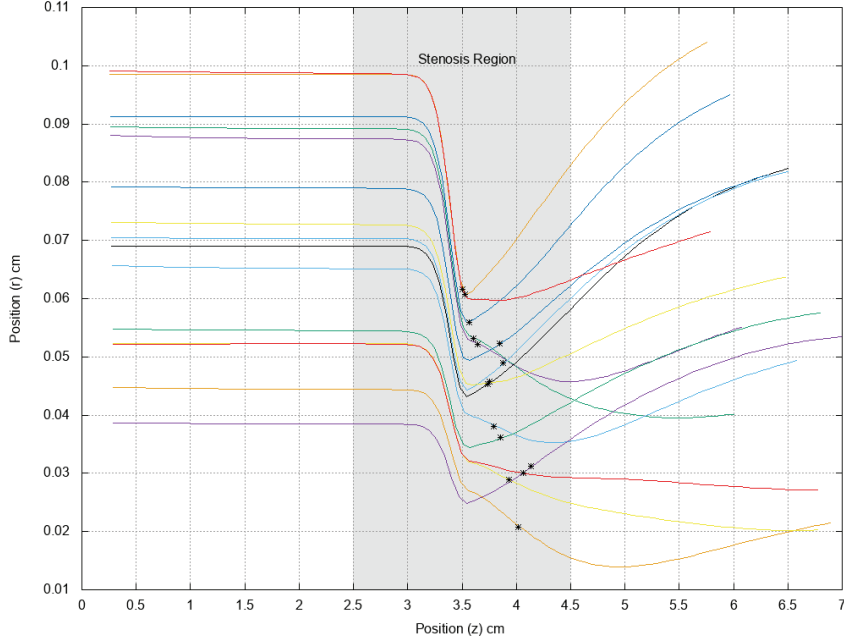Figure 6: Aggregate particle breakup into nanoparticle components.

Figure 7: Radial position as a function of position along the z-axis for aggregate particles flowing through the concentric R_1 vessel geometry with an optimal breakup threshold. The stars (*) indicate particle breakup position. Note that aggregate particles continue to be tracked through the flow as though they never broke apart even if they do breakup.

every fifth time step was captured. No biochemical nanoparticle binding components were used in this study to determine if the nanoparticles will adhere to the stenosis after breakup.

The R_1, R_2 and R_3 geometries with a concentric stenosis and 50% occlusion were tested. The specific density and aggregate particle diameter were kept constant at 1.0 and 3.8 μm, respectively. An aggregate particle diameter of 3.8 μm was chosen for consistency with Ref. [10].

For the R_1 geometry, fifteen aggregate particles were inserted into the flow to study the effect of different breakup thresholds. Thirteen different breakup thresholds, determined by scaling $\omega_{min} = 14.89\ rad/s$ for this R_1 geometry, were tested to determine the optimal value. All aggregate particles broke up within the stenosis region when the threshold value was between $3\omega_{min}$ (44.66 rad/s) and $5\omega_{min}$ (74.44 rad/s). At thresholds less than $3\omega_{min}$ (44.66 rad/s) particles broke up prematurely, while at thresholds greater than $5\omega_{min}$ (74.44 rad/s) particles did not break up. By comparing the average distance of particle breakup from the stenosis center, the optimal breakup threshold was determined to be $3\omega_{min}$ (44.66 rad/s) as seen in Figure 7. This breakup threshold yielded the closest average distance from the stenosis center (0.29 cm), with all particles breaking up after the stenosis center. Table 4 shows the results for all thirteen breakup thresholds that were tested.

It was observed that the initial particle position was correlated with the proximity of the breakup position to the stenosis center. To ensure this observance was not an

16
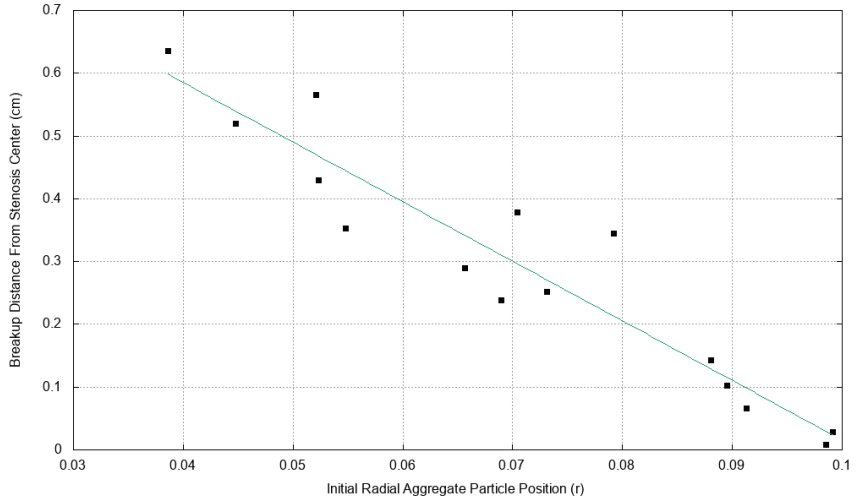
Figure 8: Breakup distance from stenosis center versus initial radial position of the aggregate particle for the concentric R_1 geometry. The line of best fit shows a negative correlation, and is represented by $\hat{y} = 0.96 - 9.49r_0$ with an R^2 value of 0.90.

Shear Threshold (ω)	Total AP	Total Broken AP	Total Broken in Stenosis Region	Avg Distance from Center (cm)
37.22	15	15	4	1.777
40.32	15	15	12	0.915
43.18	15	15	13	0.701
44.66	15	15	15	0.292
46.15	15	15	15	0.294
46.52	15	15	15	0.304
55.83	15	15	15	0.347
65.13	15	15	15	0.413
74.44	15	15	15	0.466
93.05	15	13	13	0.498
111.66	15	11	9	0.564
148.88	15	6	5	0.673
223.32	15	0	0	-

Table 4: Breakup threshold data for the R_1 geometry. Note that the shear threshold values are computed using multiples of $\omega_{min} = 14.8879598$ and then rounded to two decimals.

error caused by recording the data at every 5th time step (as opposed to recording the data at every time step), the simulation for the R_1 geometry was repeated, this time recording the data at every time step. The least squares linear regression analysis was performed to determine the relationship between the initial radial position of the particle and the proximity of the breakup to the stenosis center. For this analysis the optimal threshold (44.66 rad/s) was used with aggregate particles possessing a 3.8 μm diameter and specific density of 1. The line of best fit that emerged from the analysis is given as $\hat{y} = 0.96 - 9.49r_0$, with an R^2 value of 0.90, and where $\hat{y}$ is the predicted breakup proximity (cm) to the stenosis center, and r_0 is the initial radial particle position. The initial radial position of the aggregate particles is negatively correlated with distance from the breakup position to the stenosis center. As particles are placed into the flow, the farther their initial radial distance is from the geometry center, the closer the breakup occurs to the stenosis center as seen in Figure 8.

For the R_2 geometry, seventeen aggregate particles were inserted into the flow to study the effect of different breakup thresholds. Thirteen different breakup thresholds, determined by scaling $\omega_{min} = 5.90 \ rad/s$ for this R_2 geometry, were tested to determine the optimal value. All aggregate particles broke up within the stenosis region when the threshold value was between $23\omega_{min}$ (135.79 rad/s) and $49\omega_{min}$ (289.1 rad/s). The average distance from the stenosis center was minimized for 289.1 rad/s at 0.10 cm from the center. All but one particle broke up before the stenosis center, which is a stark difference to the R_1 geometry in which all particles broke up after the stenosis center. A similar regression analysis of initial radial position and breakup position that was completed for the R_1 geometry was conducted. However, unlike the R_1 geometry, no correlation was discovered in the curved R_2 geometry. Table 5 shows the results for all thirteen breakup thresholds that were tested.

For the R_3 geometry, ten aggregate particles were inserted into the flow to study the effect of different breakup thresholds. Thirteen different breakup thresholds, determined by scaling $\omega_{min} = 16.38 \ rad/s$ for this R_3 geometry, were tested to determine the optimal value. The maximum number of aggregate particles which broke up within the stenosis region was nine, and occurred when the threshold value was between $10\omega_{min}$ (163.84 rad/s) and $12\omega_{min}$ (196.61 rad/s). No distinct characteristics of the tenth particle were observed. The average distance from the stenosis center was minimal at a threshold value of $12\omega_{min}$ (196.61 rad/s) as shown in Figure 9. A similar regression analysis to that described previously of initial radial position and breakup position was conducted. No correlation was discovered in the curved R_3 geometry from this analysis. In contrast to the R_1 and R_2 geometries at their optimal thresholds, a slight majority (60%) of aggregate particles broke up before the stenosis center in the R_3 geometry. Table 6 shows the results for all thirteen breakup thresholds that were tested.

In summary, the curvature of vessel geometry greatly effects the optimal aggregate particle breakup threshold. The optimal breakup threshold of the R_2 was approximately 6.3 times greater than R_1, and the R_3 curved geometry was approximately 4.5 times greater than that of the R_1 straight geometry. A clear correlation between vessel curvature and optimal breakup threshold was not observed, but it can be said that curvature creates greater complexity, which this study cannot examine fully.

Shear Threshold (ω)	Total AP	Total Broken AP	Total Broken in Stenosis Region	Avg Distance from Center (cm)
44.28	17	17	1	0.992
59.04	17	17	4	0.848
118.08	17	17	9	0.489
121.03	17	17	15	0.221
123.98	17	17	16	0.211
129.89	17	17	16	0.184
135.79	17	17	17	0.150
141.70	17	17	17	0.145
177.12	17	17	17	0.129
283.39	17	17	17	0.104
289.30	17	17	17	0.103
295.20	17	16	16	0.097
324.72	17	16	16	0.097

Table 5: Breakup threshold data for the R_2 geometry. Breakup threshold data for the R_2 geometry. Note that the shear threshold values are computed using multiples of $\omega_{min} = 5.9040012962963$ and then rounded to two decimals.

Shear Threshold (ω)	Total AP	Total Broken AP	Total Broken in Stenosis Region	Avg Distance from Center (cm)
40.96	10	10	0	2.108
122.88	10	10	4	1.347
147.46	10	10	7	0.584
163.84	10	10	9	0.445
165.48	10	10	9	0.445
175.31	10	10	9	0.482
176.95	10	10	9	0.482
178.58	10	10	9	0.481
180.22	10	10	9	0.488
196.61	10	10	9	0.364
212.99	10	8	8	0.157
245.76	10	6	6	0.143
327.68	10	6	6	0.121

Table 6: Breakup threshold data for the R_3 geometry. Breakup threshold data for the R_3 geometry. Note that the shear threshold values are computed using multiples of $\omega_{min} = 16.3839233$ and then rounded to two decimals.

The optimal breakup thresholds for both curved cases was at the highest end of the optimal range of thresholds, while the straight case threshold was found at the lower end of its range. It was discovered that for the straight case, a negative correlation exists between initial aggregate particle radial position and average breakup distance from the stenosis; this pattern was not seen in the R_2 or R_3 curved cases.
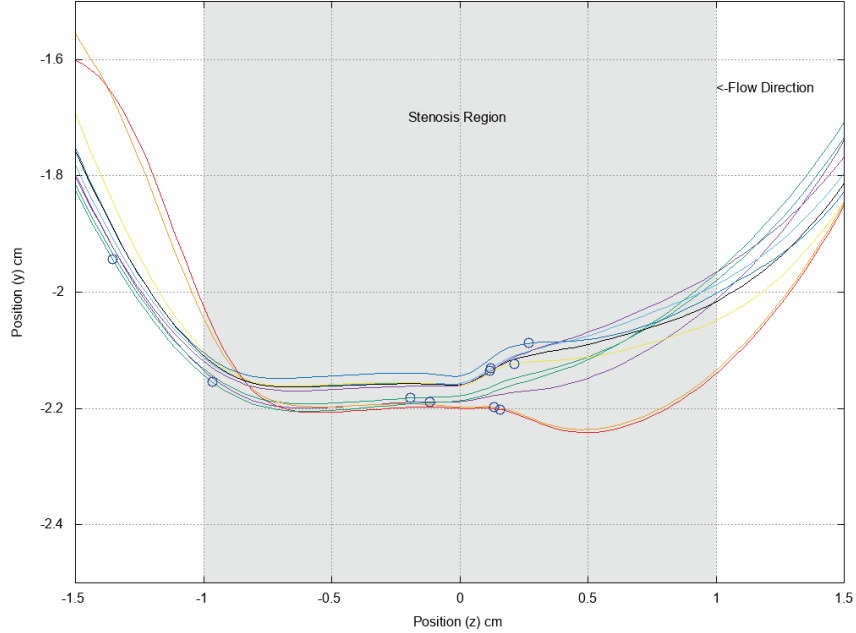

Figure 9: Radial position as a function of position along the z-axis for aggregate particles flowing through the concentric R_3 vessel geometry with an optimal breakup threshold. The circles indicate particle breakup position. Note that aggregate particles continue to be tracked through the flow as though they never broke apart even if they do breakup.

3.2   Specific Density

Specific density was tested on both the R_1 and R_3 geometries. Aggregate particle diameter and breakup threshold were kept constant at 3.8 μm and $10\omega_{min}$ respectively. Specific densities from 1 to 1.3 were tested. There was no change in the results for these cases. It was determined that in order for specific density to make any noticeable change, the specific density would have to be set to an unrealistic value of 10^4 or above.

3.3   Particle Diameter

The effect of particle diameter on breakup threshold was studied using the R_1 and R_3 geometries, both with a 50% concentric occlusion. The specific density was kept constant at 1. Optimal breakup threshold values of 44.66 rad/s for the R_1 geometry and 196.61 rad/s for the R_3 geometry were used. Three particle diameters (1.0, 3.8 and 5.0 μm) were studied for each geometry. These diameters were chosen based

on the diameter of natural platelets which lies between 1.0 and 5.0 μm, while 3.8 μm was included because it is the average diameter of fabricated SA-NT aggregate particles [10].

A positive correlation between aggregate particle diameter and average breakup distance from stenosis center was discovered for the R_1 geometry. Using regression analysis, the relationship can be described by the equation $\hat{y} = 0.292 + 0.0000887d$, with $R^2 = 0.99$, and where d is the aggregate particle diameter (μm), and $\hat{y}$ is the predicted breakup proximity (cm) to the stenosis center. Similar analysis was performed for the R_3 geometry, and a negative correlation was found with $\hat{y} = 0.454 - 0.00272d$, with $R^2 = 0.85$.

This demonstrates that curvature matters when choosing an optimal aggregate particle diameter. Smaller particles may be ideal for straight vessels and larger particles for a vessel with greater curvature. Overall the ranges of breakup distance for the R_1 and R_3 geometries respectively were 3.55×10^{-4} and 1.13×10^{-2}, so the benefit may be marginal. The positive correlation between particle size and average particle residence time found in Doig et al.'s study may warrant a larger aggregate particle diameter in order to gain the binding benefit of larger nanoparticles [9]. Table 7 shows the average distance from stenosis center for the R_1 and R_3 diameter cases that were simulated.

Diameter(μm)	R_1 Average Distance from Stenosis Center (cm)	R_3 Average Distance from Stenosis Center (cm)
1	0.29160212	0.449844683
2	0.291686948	0.449477008
3	0.291774464	0.447882889
3.8	0.29184599	0.445322032
4	0.291864522	0.443923137
5	0.291957333	0.438509313

Table 7: Aggregate Particle Diameter Data.

3.4 Stenosis Shape and Location

The R_1 geometry was tested with a 50% occluded eccentric stenosis inserted into it in order to compare it to the R_1 concentric case. The minimum angular velocity for this case was 11.66 rad/s. In order to attain a similar threshold value to the R_1 concentric case, $3.82\omega_{min}$ was used to attain a threshold of 44.66 rad/s. Sixteen aggregate particles were introduced into the flow. In this case, all particles broke up within the stenosis region. The eccentric R_1 case had an average minimum distance from stenosis center of 0.29 cm, which is identical to the concentric case to two significant digits.

The R_3 geometry was tested with 50% occluded eccentric stenoses in three positions: superior, inferior, and ventral/dorsal. The superior case had a minimum angular velocity of 1.23 rad/s. To meet the concentric case threshold, the minimum was multiplied by 159.98. Twenty particles were tested, and all particles broke up
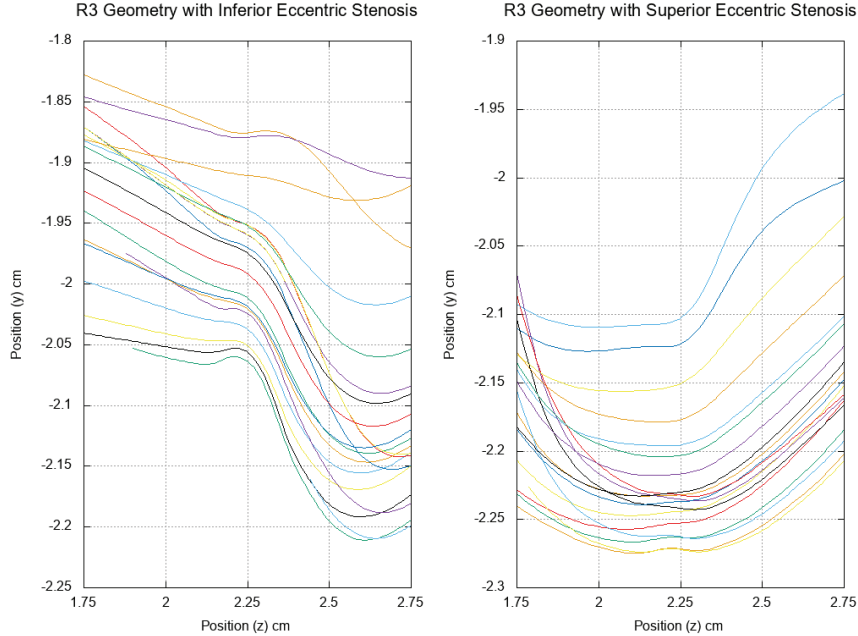
Figure 10: Position of aggregate particles flowing through R_3 geometries with inferior eccentric and superior eccentric stenoses.

within the stenosis region. The average distance from the stenosis center is 0.19 cm, which was closer than for the concentric case with the same parameters.

The inferior case had a minimum angular velocity of 2.10 rad/s. To meet the R_3 concentric case threshold, the minimum was multiplied by 93.52. Twenty particles were tested. All particles broke up within the stenosis region. The average distance from stenosis center is 0.07 cm, which is closer than for the concentric case.

The ventral/dorsal case had a minimum angular velocity of 2.74 rad/s, and in order to match the concentric case threshold of 196.61, the minimum was multiplied by 71.73 to attain the threshold. Fourteen aggregate particles passed through the flow. All particles broke up within the stenosis region, and this case had an average distance from stenosis center of 0.20 cm, which again is closer than for the concentric case.

In all R_3 eccentric cases, the particles broke up before the stenosis center, which agrees with the concentric case. All three eccentric cases fared better in both particle breakup within the stenosis region and average breakup distance from stenosis center. The inferior eccentric case performed the best due to its position relative to the particle trajectory, reminiscent of the correlation between initial particle position and breakup position shown in the R_1 concentric case. A comparison of the inferior and superior case are shown in Figure 10 for a visual of stenosis position and its effect on particle trajectory. It should be noted that all eccentric cases had a greater average particle breakup position, and all also had greater occlusion in the radial center than the concentric case. This greater center occlusion did not seem to affect the straight cases' average breakup distance. Curvature, which in part drives particle trajectory, combined with stenosis location, has a sizeable effect on optimal breakup distance.

4   Summary and Remarks

This study used computational methods to better understand how aggregate particle breakup threshold, diameter and specific density, as well as vessel curvature and stenosis shape affect the efficiency of shear-activated nanotherapeutics in the treatment of atherosclerosis. Different idealized geometries were used to test and analyze these parameters. Optimal angular velocity breakup thresholds were discovered for both straight and curved geometry cases. Geometry curvature was a sizeable factor in breakup threshold, as the curved vessel cases (R_2, R_3) required 6.3 and 4.5 times the angular velocity of the straight vessel, respectively. No clear pattern was shown relating vessel curvature and optimal breakup threshold.

In the straight geometry cases, a correlation was found between initial particle position and particle breakup proximity to the stenosis center. As particles are positioned farther away from the vessel center, their breakup proximity from center is decreased. A similar correlation was not found in the curved vessel cases.

Aggregate particle diameter was also explored. Diameters from 1.0 to 5.0 μm were used for both straight and curved geometries. Small decreases in average particle breakup distance from stenosis center were seen as particle diameters decreased for the straight vessel case. The opposite happened with the curved vessel case. As the particle diameter increased, a slight decrease in average particle breakup distance from stenosis was achieved. This indicates that as vessel curvature increases, so should the diameter of the aggregate particle for optimal results.

Different specific densities were tested for both straight and curved geometries. It was determined that specific density will not play a role in efficiency of shear-activated nanotherapeutics. Stenosis shape and location were tested in both the straight vessel and one of the curved vessel geometries. Curvature in conjunction with stenosis location had a great effect on average breakup distance from the stenosis center. This is a similar observation to the initial particle position correlation found in the R_1 cases. Both indicate that it is optimal to have the stenosis in the aggregate particle path.

Further studies need to be conducted to find optimal parameters. Effects of greater occlusions and more complicated geometries might give us more insight and a better understanding of the effectiveness of shear activated nanotherapeutics. There is evidence that blood viscosity is a risk factor for atherosclerosis; therefore, studies should be conducted using greater blood viscosity than used in this study to determine its effect on particle breakup [20].

References

[1] T. E. Nogles and M. A. Galuska, "Middle cerebral artery stroke," StatPearls, 2021 Jan.

[2] "Stroke facts," Centers for Disease Control & Prevention, 2020. Accessed: 2021-03-29.

[3] N. P. Denswil, A. C. Van der Wal, K. Ritz, O. J. de Boer, E. Aronica, D. Troost, and M. J. Daemen, "Atherosclerosis in the Circle of Willis: Spatial differences in composition and in distribution of plaques in applied dynamical systems," Atherosclerosis, vol. 251, no. 4, pp. 78–84, 2016 Aug.

[4] "Circle of Willis: Medlineplus medical encyclopedia," MedlinePlus, U.S. National Library of Medicine. Accessed: 2021-03-29.

[5] A. E. Roher, C. Esh, T. A. Kokjohn, W. Kalback, D. C. Luehrs, J. D. Seward, L. I. Sue, and T. G. Beach, "Circle of Willis atherosclerosis is a risk factor for sporadic Alzheimer's disease," Arteriosclerosis, Thrombosis, and Vascular Biology, vol. 23, no. 11, pp. 2055–2062, 2003 Nov.

[6] B. Flusty, A. de Havenon, S. Prabhakaran, D. S. Liebeskind, and S. Yaghi, "Intracranial atherosclerosis treatment: Past, present, and future," Stroke, vol. 51, 2020 Feb.

[7] R. Olie, P. van der Meijden, H. M. H. Spronk, and H. T. Cate, "Antithrombotic therapy: Prevention and treatment of atherosclerosis and atherothrombosis," Handbook of Experimental Pharmacology, 2020.

[8] "Statin side effects: Weigh the benefits and risks," Mayo Clinic, Mayo Foundation for Medical Education and Research, 2020. Accessed: 2021-03-29.

[9] G. Doig, G. H. Yeoh, V. Timchenko, G. Rosengarten, T. J. Barber, and S. C. Cheung, "Simulation of blood flow and nanoparticle transport in a stenosed carotid bifurcation and pseudo-arteriole," The Journal of Computational Multiphase Flows, vol. 4, no. 1, pp. 85–101, 2012 Mar.

[10] N. Korin, M. Kanapathipillai, B. D. Matthews, and M. Crescente, "Shear-activated nanotherapeutics for drug targeting to obstructed blood vessels," Science, vol. 337, no. 6095, pp. 738–742, 2012 Jul.

[11] M. G. Marosfoi, N. Korin, M. J. Gounis, O. Uzun, S. Veantham, E. T. Langan, A.-L. Papa, O. W. Brooks, C. Johnson, A. S. Puri, D. Bhatta, M. Kanapathipillai, B. R. Bronstein, J.-Y. Chueh, D. E. Ingber, and A. K. Wakhloo, "Shear-activated nanoparticle aggregates combined with temporary endovascular bypass to treat large vessel occlusion," Stroke, vol. 46, no. 12, pp. 3507–3513, 2015 Oct.

[12] "The crucial, controversial carotid artery part I: The artery in health and disease," Harvard Health, 2011 Aug. Accessed: 2021-03-29.

[13] "Carotid artery disease," Johns Hopkins Medicine. Accessed: 2021-03-29.

[14] "Freecad." https://www.freecadweb.org/.

[15] R. Löhner, "Automatic unstructured grid generators," Finite Elements in Analysis and Design, vol. 25, pp. 111–134, 1997.

24

[16] R. Löhner, "Renumbering strategies for unstructured grid solvers operating on shared memory, cached based parallel machines," Computer Methods in Applied Mechanics and Engineering, vol. 163, pp. 95–109, 1998.

[17] J. Cebral, "Image-based computational hemodynamics methods and their application for the analysis of blood flow past endovascular devices, in biomechanical systems technology: (1) computational methods," World Scientific, pp. 29–85, 2007.

[18] F. Mut, "Fast numerical solutions of patient-specific blood flows in 3D arterial systems," Int. J. Num. Meth. Biomed. Eng., vol. 26, no. 1, pp. 73–85, 2010.

[19] B. Chung, D. Platt, and A. Vaidya, "The mechanics of clearance in a non-Newtonian lubrication layer," International Journal of Non-Linear Mechanics, vol. 86, pp. 133–145, 2016.

[20] R. C. Becker, "The role of blood viscosity in the development and progression of coronary artery disease," Cleveland Clinic Journal of Medicine, vol. 60, no. 5, pp. 53–358, 1993 Sep.